Materials Advances

ROYAL SOCIETY OF CHEMISTRY

PAPER

View Article Online
View Journal | View Issue

Cite this: *Mater. Adv.*, 2025, 6, 6445

First-principles evaluation of the elastic properties of crystalline Li-ion conductors

Masato Torii, Atsushi Sakuda,* Kota Motohashi and Akitoshi Hayashi

All-solid-state batteries have emerged as alternative rechargeable batteries offering high energy density and enhanced safety. However, suppressing their mechanical degradation is challenging. In particular, inorganic solid electrolytes must form mechanically stable solid–solid interfaces with electrode active materials, making the examination of their elastic properties essential for creating robust interfaces. Pugh's ratio (*B*/*G*) serves as a key parameter for estimating ductility, with a desirable value exceeding 1.75—a criterion originally proposed for polycrystalline metals. In this study, the elastic properties of Li-ion-conducting crystalline electrolytes were comprehensively evaluated *via* first-principles calculations. The calculated mechanical properties of their crystal structures were classified based on their anion elements. The elastic moduli of sulfide and halide crystals were relatively lower than those of oxide and nitride materials. The Pugh ratios of sulfide crystals were generally higher than 1.75, while those of oxide crystals clustered around 1.75 and nitride crystals typically fell below this threshold. Additionally, a nonlinear correlation between mean atomic volume and elastic constants was observed. Among the various electrolytes, Li_2SO_4 exhibited exceptional elastic properties: α-Li_2SO_4 demonstrated a significantly high *B*/*G* value of 4.28, indicating distinctive ductility.

Received 9th July 2025,
Accepted 4th August 2025

DOI: 10.1039/d5ma00733j

rsc.li/materials-advances

1. Introduction

All-solid-state batteries are anticipated as alternative rechargeable batteries offering high energy density and enhanced safety.[1–3] However, challenges persist, particularly degradation at the solid–solid interface between electrode active materials and solid electrolytes. Mechanical degradation, a key issue, arises from the expansion and contraction of electrode active materials during charge and discharge cycles. This volumetric change generates cracks and voids within the electrode active materials and solid electrolytes at their interface.[4] To mitigate mechanical degradation, solid electrolytes must exhibit sufficient mechanical flexibility to accommodate the volumetric changes of electrode active materials.

Solid electrolytes are classified primarily based on their anion elements and crystal unit cell structures. Sulfide solid electrolytes are notable for their high moldability and ionic conductivity.[5] They exhibit superior formability and can be densified solely by pressing under ambient temperature.[6] Among sulfide solid electrolytes, Li-ion conductors such as $Li_{10}GeP_2S_{12}$ (LGPS) type electrolytes demonstrate the highest ionic conductivity, exceeding 10^{-2} S cm^{-1}.[2,7,8] The argyrodite Li_6PS_5Cl crystal family is another typical sulfide solid electrolyte, with ionic conductivity reaching 10^{-2} S cm^{-1}.[9,10]

Oxide solid electrolytes are also widely used due to their electrochemical stability. Garnet-type $Li_7La_3Zr_2O_{12}$ (LLZO) exhibits both high ionic conductivity (~1 mS cm^{-1}) and stability against lithium Li metal.[11,12] Some nitride solid electrolytes also possess high ionic conductivity; for instance, Li_3N electrolytes exceed 10^{-3} S cm^{-1}.[13] Recently, halide solid electrolytes have garnered attention because of their high ionic conductivity and oxidation resistance. Asano *et al.* first reported the novel Li_3YCl_6 chloride electrolyte, which exhibited ionic conductivity exceeding 10^{-3} S cm^{-1}.[14] Following this discovery, a variety of Li_3MCl_6-type chloride electrolytes have been investigated.[15]

From a mechanical perspective, solid electrolytes must possess adequate deformability and ductility to accommodate the expansion and contraction of electrode active materials, thereby minimizing stress accumulation at the interface. The elastic modulus is a fundamental property that quantifies the resistance of a material against deformation under microscopic elastic strain. During elastic deformation, stress and strain are proportional, with the elastic modulus serving as the proportionality constant. In general, a lower elastic modulus corresponds to easier deformation, making solid electrolytes with low elastic moduli preferable for such applications.

Various proportional constants are defined based on the plane and direction of stress and strain, and this information is typically organized in a four-dimensional elastic tensor.

Department of Applied Chemistry, Graduate School of Engineering, Osaka Metropolitan University, 1-1 Gakuen-cho, Naka-ku, Sakai, Osaka 599-8531, Japan. E-mail: saku@omu.ac.jp; Fax: +81-72-2549910; Tel: +81-72-2549331

For ease of interpretation or computation, this tensor is often reduced to a two-dimensional form. The Voigt–Reuss–Hill approximation is commonly employed to predict elastic moduli from the tensor components.[16] The primary elastic moduli used for evaluating crystalline materials include the polycrystalline Young's modulus (E), bulk modulus (B), and shear modulus (G). Young's modulus represents the proportionality constant between stress and strain in the uniaxial direction, while the polycrystalline Young's modulus (E) provides an averaged value for polycrystalline materials. The bulk modulus (B) quantifies the relationship between isotropic stress and volumetric strain, whereas the shear modulus (G) is related to angular displacement under equilibrium shear force. Additionally, Poisson's ratio (ν), defined as the ratio of transverse strain to axial strain in response to uniaxial stress, is often used for mechanical characterization.

Pugh's ratio, the shear-to-bulk modulus ratio (B/G), is a key parameter for evaluating the mechanical ductility of solid electrolytes.[17,18] Originally proposed by Pugh in the context of polycrystalline metals, this criterion assesses a material's ability to undergo plastic deformation.[17] Plastic deformation occurs when a material is strained beyond its elastic limit, and its likelihood depends on the material's elastic properties. Pugh suggests that polycrystalline metal materials, with a B/G ratio exceeding 1.75, are more likely to exhibit plastic deformation. However, this standard, derived for metals, has not been validated for ceramic materials, such as those used in inorganic solid electrolytes.

Deng *et al.* previously conducted a comprehensive investigation of the elastic moduli of typical solid electrolytes,[19] *viz.* alkali superionic conductors, using first-principles calculations, uncovering trends influenced by anion species, structural frameworks, and alkali ions. Nevertheless, they did not include nitrides or the more recently explored chloride solid electrolytes.[14,15] Furthermore, additional investigations on a wider range of electrolytes, beyond those covered in their study, are required.

In this study, we aimed to provide more comprehensive insights into the elastic properties of Li-ion conductors by examining a broader selection of electrolyte materials. The calculated elastic moduli are systematically categorized based on the anion types and crystal structures of the solid electrolytes. Using these findings, alongside an analysis of Pugh's ratio (B/G), the study identifies solid electrolytes with high deformability and ductility, which are essential for accommodating the expansion and contraction of electrodes.

2. Computational details

The elastic properties of crystal structures were calculated computationally using density functional theory (DFT).[20,21] All DFT calculations were performed with the Vienna Ab initio Simulation Package (VASP),[22,23] employing the generalized gradient approximation (GGA) exchange–correlation functional as formulated by Perdew–Burke–Ernzerhof (PBE).[24,25] The projected augmented wave (PAW) method[26,27] was used to describe the pseudopotentials of inner-shell electrons. A cut-off energy of 500 eV was applied for the plane wave basis set, which was higher than the maximum ENMAX among all elements present in the solid electrolytes used in this study. The electronic energy convergence criterion was set at 10^{-6} eV.

The Monkhorst–Pack scheme[28] was utilized to determine k-point distributions and the irreducible Brillouin zone. As an exception, a Γ-centered $1 \times 1 \times 1$ k-point mesh was adopted for LLZO due to computational cost considerations. Lattice constants and ionic positions of ordinary crystal structures were fully relaxed, ensuring that the final forces on all relaxed atoms were less than 0.01 eV Å^{-1}. On-site Coulomb term (U) values of 2.50, 3.50, 4.00, and 2.30 eV were applied for the Ti-3d, Zr-4d, Nb-4d, and La-5f orbitals, respectively, following prior studies.[29–32] We incorporated the effect of van der Waals interactions by applying the DFT-D3 method with the Becke–Johnson damping function to all calculations.[33] Spin polarization was not considered in the computations. The ''mean atomic volume'' (MAV) was defined as the ratio of the cell volume to the total number of atoms, with the cell volume determined from lattice constants obtained through structural optimization in this study.

Elastic moduli were determined from the computational results of elastic tensors calculated using the Voigt–Reuss–Hill approximation methods.[16] The bulk modulus (B) and shear modulus (G) are obtained as the average values (the Hill's prediction values) of those calculated using the Voigt's (B_V and G_V) and the Reuss's (B_R and G_R) prediction methods (eqn (1)–(6)). In these equations, each component of the inverse elasticity tensor is represented by S_{ij}. The polycrystalline Young's modulus (E) and Poisson's ratio (ν) were estimated using eqn (7) and (8), respectively.

$$9B_V = (C_{11} + C_{22} + C_{33}) + 2(C_{12} + C_{23} + C_{31}) \quad (1)$$

$$1/B_R = (S_{11} + S_{22} + S_{33}) + 2(S_{12} + S_{23} + S_{31}) \quad (2)$$

$$B = (B_V + B_R)/2 \quad (3)$$

$$15G_V = (C_{11} + C_{22} + C_{33}) - (C_{12} + C_{23} + C_{31}) + 3(C_{44} + C_{55} + C_{66}) \quad (4)$$

$$15/G_R = 4(S_{11} + S_{22} + S_{33}) - 4(S_{12} + S_{23} + S_{31}) + 3(S_{44} + S_{55} + S_{66}) \quad (5)$$

$$G = (G_V + G_R)/2 \quad (6)$$

$$E = 9BG/(3B + G) \quad (7)$$

$$\nu = (3B - 2G)/2(3B + G) \quad (8)$$

These elastic properties were extracted from the elastic tensors using VASPKIT.[34] Notably, these calculations were conducted by assuming a temperature of 0 K.

In some of the electrolytes investigated in this study, certain Li sites exhibit partial occupancies or disorder. While such site occupancies can influence the calculated elastic properties, the Li positions with the highest occupancies and/or highest symmetry were selected for the structural models used in the

calculations. This approach was adopted to ensure a consistent and representative comparison across different materials.

3. Selection of solid electrolyte materials

In this section, the solid electrolytes selected for elastic constant calculations are discussed.

For the argyrodite-type structures, Li_6PS_5Cl, Li_6PS_5Br, Li_6PS_5I, and Li_6SbS_5I were selected. Li_6PS_5Br and Li_6PS_5I were included because Br and I are commonly used as halogens alongside Cl.[9] Li_6SbS_5I, an argyrodite material previously reported by our group, demonstrated an ionic conductivity of 2.1×10^{-6} S cm^{-1}, which was higher than that of Li_6PS_5I.[35]

For LGPS-type structures, $Li_{10}GeP_2S_{12}$, $Li_{10}SnP_2S_{12}$ and $Li_{10}SiP_2S_{12}$ were selected. Additionally, several thio-LISICON-type electrolytes, including Li_xXS_4 solid electrolytes (X = B, Al, Si, Ga, Ge, Sn, and Sb),[36–42] were included as sulfide solid electrolytes. These materials can serve as solid electrolytes themselves or as end members for other electrolytes, such as LGPS-type materials. $Li_4P_2S_6$ was also included as a relatively stable solid electrolyte, maintaining its crystal structure up to 950 °C in vacuum and 280 °C in air.[43] The low-temperature (LT) phase of Li_7PS_6 was introduced as another argyrodite electrolyte.[44]

Beyond garnet-type structures, various oxide electrolytes with high ionic conductivities[45] were considered, including Na super-ionic conductor (NASICON)-type $LiM_2(PO_4)_3$ electrolytes (M = Ti, Ge, Zr, and Hf),[46] Li super-ionic conductor (LISICON)-type Li_2ZnGeO_4 electrolyte,[47] lithium phosphorus oxynitride (LiPON) electrolytes such as Li_2PNO_2,[48] perovskite electrolytes ($Li_{1/8}La_{5/8}TiO_3$ and $Li_{1/2}La_{1/2}TiO_3$),[49] and anti-perovskite electrolytes (Li_3OCl, Li_3OBr, and $Li_3OCl_{0.5}Br_{0.5}$).[50] *ortho*-Oxyacid electrolytes such as Li_3PO_4 and Li_2SO_4, although generally exhibiting low ionic conductivities, were also considered. Our previous studies reported electrolytes in the Li_3BO_3–Li_2SO_4[51] and Li_4GeO_4–Li_3VO_4[52] systems using *ortho*-oxyacid electrolytes as end members.

Nitride electrolytes other than Li_3N include $LiSi_2N_3$, Li_7PN_4, and $LiPN_2$.[53,54] Halide electrolytes such as $LiAlCl_4$, Li_2CdCl_4, Li_2MgCl_4, and Li_2ZnI_4[55–57] were studied alongside Li_3YCl_6.[14] Li_3MCl_6-based electrolytes for various M elements have also been explored, with Li_3InCl_6 often used together with Li_3YCl_6 owing to its high ionic conductivity.[58] These solid electrolyte materials were selected based on a previously reported review on their ionic conductivities.[59]

To calculate the elastic properties of these materials, input structural files were primarily obtained from the Materials Project[60] or the ICSD database.[61] The exception was the input file for the Li_6SbS_5I crystal structure, which was separately created based on the Li_6PS_5Cl structure.

4. Results and discussion

The calculated elastic moduli for various sulfide, oxide, and other electrolyte crystal structures are summarized in

Table 1 Crystal structure details and calculated elastic constants of various sulfide electrolytes

Type	Formula	Space group	Crystal system	E/GPa	B/GPa	G/GPa	ν	B/G	MAV/cm^3 mol^{-1}	Ref.
Argyrodite	Li_6PS_5Cl	$F\bar{4}3m$	Cubic	22.1	28.7	8.1	0.37	3.54	No data	19
Argyrodite	Li_6PS_5Br	$F\bar{4}3m$	Cubic	25.3	29.0	9.3	0.35	3.11	No data	19
Argyrodite	Li_6PS_5I	$F\bar{4}3m$	Cubic	30.0	29.9	11.3	0.33	2.65	No data	19
Argyrodite	Li_6PS_5Cl	$F\bar{4}3m$	Cubic	27.44	34.73	10.03	0.37	3.46	11.74	This study
Argyrodite	Li_6PS_5Br	$F\bar{4}3m$	Cubic	30.11	35.19	11.09	0.36	3.17	11.75	This study
Argyrodite	Li_6PS_5I	$F\bar{4}3m$	Cubic	35.10	35.14	13.16	0.33	2.67	11.88	This study
Argyrodite	Li_6SbS_5I	$F\bar{4}3m$	Cubic	38.27	32.88	14.65	0.31	2.24	12.87	This study
Thio-LISICON (LGPS-type)	$Li_{10}GeP_2S_{12}$	$P4_2mc$	Tetragonal	37.2	30.4	14.4	0.30	2.12	11.59	61
Thio-LISICON (LGPS-type)	$Li_{10}GeP_2S_{12}$	$P4_2mc$	Tetragonal	21.7	27.3	7.9	0.37	3.46	No data	19
Thio-LISICON (LGPS-type)	$Li_{10}SnP_2S_{12}$	$P4_2mc$	Tetragonal	29.1	23.5	11.2	0.29	2.10	No data	19
Thio-LISICON (LGPS-type)	$Li_{10}SiP_2S_{12}$	$P4_2mc$	Tetragonal	24.8	27.8	9.2	0.35	3.02	No data	19
Thio-LISICON (LGPS-type)	$Li_{10}GeP_2S_{12}$	$P4_2mc$	Tetragonal	28.03	32.40	10.34	0.36	3.13	10.89	This study
Thio-LISICON (LGPS-type)	$Li_{10}SnP_2S_{12}$	$P4_2mc$	Tetragonal	26.01	30.97	9.56	0.36	3.24	11.14	This study
Thio-LISICON (LGPS-type)	$Li_{10}SiP_2S_{12}$	$P4_2mc$	Tetragonal	28.21	32.74	10.40	0.36	3.15	10.77	This study
Thio-LISICON	β-Li_3PS_4	$Pnma$	Orthorhombic	29.5	23.3	11.4	0.29	2.04	No data	19
Thio-LISICON	γ-Li_3PS_4	$Pmn2_1$	Orthorhombic	33.4	32.9	12.6	0.33	2.61	No data	19
Thio-LISICON	β-Li_3PS_4	$Pnma$	Orthorhombic	33.49	29.28	12.79	0.30	2.29	11.34	This study
Thio-LISICON	γ-Li_3PS_4	$Pmn2_1$	Orthorhombic	36.82	39.34	13.70	0.34	2.87	11.23	This study
Thio-LISICON	Li_4SnS_4	$Pnma$	Orthorhombic	42.90	38.45	16.32	0.31	2.36	11.30	This study
Thio-LISICON	Li_4GeS_4	$Pnma$	Orthorhombic	46.42	40.73	17.72	0.31	2.30	10.65	This study
Thio-LISICON	Li_5AlS_4	$P2_1/m$	Monoclinic	61.46	43.55	24.3	0.26	1.79	9.36	This study
Thio-LISICON	Li_3BS_3	$Pnma$	Orthorhombic	35.96	30.16	13.82	0.30	2.18	10.15	This study
Thio-LISICON	Li_5GaS_4	$P2_1/m$	Monoclinic	59.65	43.17	23.49	0.27	1.84	9.45	This study
Thio-LISICON	Li_3SbS_4	$Pmn2_1$	Orthorhombic	33.86	35.48	12.62	0.34	2.81	12.57	This study
Other sulfides	$Li_7P_3S_{11}$	$P\bar{1}$	Triclinic	21.9	23.9	8.1	0.35	2.95	No data	19
Other sulfides	$Li_7P_3S_{11}$	$P\bar{1}$	Triclinic	28.37	29.52	10.59	0.34	2.79	11.39	This study
Other sulfides	Li_7PS_6	$Pna2_1$	Orthorhombic	51.88	41.15	20.11	0.29	2.05	9.95	This study
Other sulfides	$Li_4P_2S_6$	$P\bar{3}m1$	Trigonal	81.50	46.14	33.80	0.21	1.37	9.99	This study
Other sulfides	Li_2SiS_3	$Cmc2_1$	Orthorhombic	47.91	44.53	18.14	0.32	2.45	11.28	This study
Other sulfides	Li_2SnS_3	$C2/c$	Monoclinic	92.23	51.41	38.40	0.20	1.34	10.47	This study

Table 2 Crystal structure details and elastic constants of various oxide electrolytes

Type	Formula	Space group	Crystal system	E/GPa	B/GPa	G/GPa	ν	B/G	MAV/cm^3 mol^{-1}	Ref.
ortho-Oxyacid	γ-Li_3PO_4	*Pnma*	Orthorhombic	103.4	72.5	40.9	0.26	1.77	No data	19
ortho-Oxyacid	γ-Li_3PO_4	*Pnma*	Orthorhombic	114.23	82.32	45.02	0.27	1.83	5.82	This study
ortho-Oxyacid	β-Li_3PO_4	$Pmn2_1$	Orthorhombic	118.56	83.40	46.93	0.26	1.78	5.71	This study
ortho-Oxyacid	α-Li_2SO_4	$F\bar{4}3m$	Cubic	26.77	41.19	9.62	0.39	4.28	9.61	This study
ortho-Oxyacid	β-Li_2SO_4	$P2_1/c$	Monoclinic	50.36	40.92	19.44	0.29	2.10	6.92	This study
ortho-Oxyacid	Li_3BO_3	$P2_1/c$	Monoclinic	120.49	87.31	47.44	0.27	1.84	4.47	This study
ortho-Oxyacid	Li_3VO_4	$Pmn2_1$	Orthorhombic	93.64	72.93	36.41	0.29	2.00	6.25	This study
ortho-Oxyacid	Li_4GeO_4	*Cmcm*	Orthorhombic	137.49	94.91	54.62	0.26	1.74	5.69	This study
ortho-Oxyacid	Li_4SiO_4	$P\bar{1}$	Triclinic	146.80	91.08	59.61	0.23	1.53	5.40	This study
ortho-Oxyacid	Li_4SiO_4	$P2_1/m$	Monoclinic	127.91	88.39	50.81	0.26	1.74	5.39	This study
ortho-Oxyacid	Li_5AlO_4	*Pbca*	Orthorhombic	143.72	93.98	57.71	0.24	1.63	5.45	This study
LISICON	Li_2ZnGeO_4	*Pc*	Monoclinic	115.16	91.82	44.60	0.30	2.06	6.55	This study
Oxynitride	Li_2PNO_2	$Cmc2_1$	Orthorhombic	160.02	100.65	64.78	0.24	1.55	5.66	This study
Garnet	$Li_7La_3Zr_2O_{12}$	$I4_1/acd$	Tetragonal	175.1	127.4	68.9	0.27	1.85	No data	19
Garnet	$Li_5La_3Nb_2O_{12}$	$Ia\bar{3}d$	Cubic	141.1	111.3	54.8	0.29	2.03	No data	19
Garnet	$Li_5La_3Ta_2O_{12}$	$Ia\bar{3}d$	Cubic	144.2	112.0	56.1	0.29	2.00	No data	19
Garnet	$Li_{6.25}Al_{0.25}La_3Zr_2O_{12}$	$Ia\bar{3}d$	Cubic	162.6	112.4	64.6	0.26	1.74	No data	62
Garnet	$Li_{6.5}La_3Zr_{1.5}Ta_{0.5}O_{12}$	$Ia\bar{3}d$	Cubic	154.9	99.2	62.5	0.24	1.59	No data	62
Garnet	$Li_7La_3Zr_2O_{12}$	$I4_1/acd$	Tetragonal	165.37	120.54	65.04	0.27	1.85	6.85	This study
Garnet	$Li_5La_3Nb_2O_{12}$	$Ia\bar{3}d$	Cubic	133.67	106.52	51.78	0.29	2.06	7.66	This study
Garnet	$Li_5La_3Ta_2O_{12}$	$Ia\bar{3}d$	Cubic	141.93	112.40	55.03	0.29	2.04	7.54	This study
NASICON	$LiTi_2(PO_4)_3$	$R\bar{3}c$	Trigonal	143.7	95.0	57.6	0.25	1.65	No data	19
NASICON	$LiTi_2(PO_4)_3$	$R\bar{3}c$	Trigonal	146.16	100.62	58.10	0.26	1.73	7.45	This study
NASICON	$LiGe_2(PO_4)_3$	$R\bar{3}c$	Trigonal	183.79	121.42	73.65	0.25	1.65	6.90	This study
NASICON	$LiZr_2(PO_4)_3$	$R\bar{3}c$	Trigonal	105.33	78.26	41.28	0.28	1.90	8.41	This study
NASICON	$LiHf_2(PO_4)_3$	$R\bar{3}c$	Trigonal	122.81	85.83	48.68	0.26	1.76	8.14	This study
Perovskite	$Li_{1/8}La_{5/8}TiO_3$	*Pmm*2	Orthorhombic	233.9	179.0	91.2	0.28	1.96	No data	19
Perovskite	$Li_{1/2}La_{1/2}TiO_3$	*P*2/*c*	Monoclinic	262.5	183.5	104.0	0.26	1.76	No data	19
Perovskite	$Li_{1/8}La_{5/8}TiO_3$	*Pmm*2	Orthorhombic	220.64	165.6	86.33	0.28	1.92	7.57	This study
Perovskite	$Li_{1/2}La_{1/2}TiO_3$	*P*2/*c*	Monoclinic	270.36	170.75	109.4	0.24	1.56	7.18	This study
Anti-perovskite	Li_3OCl	$Pm\bar{3}m$	Cubic	99.7	55.7	41.5	0.20	1.34	No data	19
Anti-perovskite	Li_3OBr	$Pm\bar{3}m$	Cubic	92.8	52.3	38.5	0.20	1.36	No data	19
Anti-perovskite	Li_3OCl	$Pm\bar{3}m$	Cubic	113.89	62.22	47.65	0.19	1.31	6.63	This study
Anti-perovskite	Li_3OBr	$Pm\bar{3}m$	Cubic	108.80	59.62	45.49	0.20	1.31	7.14	This study
Anti-perovskite	$Li_3OCl_{0.5}Br_{0.5}$	$Pm\bar{3}m$	Cubic	110.85	60.78	46.34	0.20	1.31	6.9	This study

Tables 1, 2, and 3, respectively. These tables also incorporate previously reported data from select studies.[15,19,62,63] The lattice constants obtained after structural optimization at 0 K are provided in Table S1.

Sulfide electrolytes exhibited generally low elastic moduli and high B/G ratios, indicating their high deformability and ductility. Specifically, the majority of their elastic moduli—E, B, and G—were below 50, 40, and 20 GPa, respectively. Moreover, most of their Pugh's ratios (B/G) exceeded the critical value of 1.75, which is commonly used to differentiate between brittle and ductile materials. These findings underscore the inherent deformability and ductility of sulfide electrolytes. Among them, argyrodite-type and LGPS-type electrolytes displayed notably low elastic moduli and B/G ratios exceeding 2.5 (except for Li_6SbS_5I, with B/G = 2.24). Particularly, their shear moduli (G) were remarkably low (<15.0 GPa), signifying a high likelihood of plastic deformation within their crystal structures. Additionally, materials such as β-Li_3PS_4, Li_3BS_3, Li_3SbS_4, and $Li_7P_3S_{11}$ demonstrated relatively low elastic moduli, with γ-Li_3PS_4, Li_3SbS_4, and $Li_7P_3S_{11}$ exhibiting B/G values of approximately 2.8.

Table 3 Crystal structure information and elastic constants of various nitride and halide electrolytes

Type	Formula	Space group	Crystal system	E/GPa	B/GPa	G/GPa	ν	B/G	MAV/cm^3 mol^{-1}	Ref.
Nitride	α-Li_3N	*P*6/*mmm*	Hexagonal	105.79	65.83	42.93	0.23	1.53	6.24	This study
Nitride	β-Li_3N	$P6_3/mmc$	Hexagonal	120.43	70.18	49.60	0.21	1.41	5.18	This study
Nitride	Li_3BN_2	$P4_2/mnm$	Tetragonal	140.51	83.64	57.59	0.22	1.45	5.36	This study
Nitride	Li_7PN_4	$P\bar{4}3n$	Cubic	221.44	105.52	96.26	0.15	1.10	4.83	This study
Nitride	$LiSi_2N_3$	$Cmc2_1$	Orthorhombic	300.80	167.44	125.27	0.20	1.34	5.79	This study
Nitride	$LiPN_2$	$I\bar{4}2d$	Tetragonal	254.93	149.84	104.78	0.22	1.43	5.51	This study
Chloride	Li_3YCl_6	$P\bar{3}m1$	Trigonal	41.9	28.9	16.6	No data	1.74	No data	15
Chloride	Li_3InCl_6	$P\bar{3}m1$	Trigonal	44.5	30.3	17.7	No data	1.71	No data	15
Chloride	Li_3YCl_6	$P\bar{3}m1$	Trigonal	41.05	28.41	16.30	0.26	1.74	12.54	This study
Chloride	Li_3InCl_6	$P\bar{3}m1$	Trigonal	43.13	29.80	17.13	0.26	1.74	12.04	This study
Chloride	$LiAlCl_4$	$P2_1/c$	Monoclinic	20.37	13.45	8.16	0.25	1.65	14.05	This study
Chloride	Li_2CdCl_4	*Imma*	Orthorhombic	33.00	33.19	12.37	0.33	2.68	12.61	This study
Chloride	Li_2MgCl_4	*Imma*	Orthorhombic	37.53	34.57	14.23	0.32	2.43	11.73	This study
Iodide	Li_2ZnI_4	*Pnma*	Orthorhombic	26.46	16.42	10.74	0.23	1.53	17.99	This study

Conversely, exceptions such as $Li_4P_2S_6$ and monoclinic Li_2SnS_3 exhibited relatively high elastic moduli. The polycrystalline Young's moduli E for these materials reached 81.50 and 92.23 GPa, respectively, whereas their shear moduli (G) were 33.80 and 38.40 GPa. These values were significantly higher than those of other sulfide materials and more than twice as high as those of argyrodite and LGPS-type materials. Despite their elevated shear modulus, their bulk moduli were only marginally larger than those of other sulfide materials ($Li_4P_2S_6$: 46.14 GPa, Li_2SnS_3: 51.41 GPa). This combination of a relatively high shear modulus and moderate bulk modulus yielded a Pugh's ratio of <1.5. Similarly, Li_5AlS_4 and Li_5GaS_4 also exhibited relatively high elastic moduli and a low B/G ratio of approximately 1.75. Overall, Pugh's ratios among sulfide electrolytes tend to be highest for materials belonging to the argyrodite and LGPS-type families. In contrast, the other thio-LISICON materials exhibit moderately high values, yet generally lower than those of argyrodite and LGPS. In addition, the other sulfide systems typically show even lower Pugh's ratios.

To validate our computational results, we compared them with elastic moduli experimentally determined *via* ultrasonic pulse-echo measurements. We have previously measured the elastic moduli of four amorphous materials synthesized through mechanical milling: Li_3PS_4, $Li_7P_3S_{11}$, Li_2SiS_3, and Li_4GeS_4. These results are summarized in Table S2. Although the experimentally observed trend in elastic moduli is generally consistent with the computational predictions, the absolute values obtained from experiments are lower than those calculated. This discrepancy is likely due to three primary contributing factors: (1) amorphous materials typically exhibit larger mean atomic volumes due to the presence of free volume; (2) the relative density (*i.e.*, packing density) of the pelletized samples is below 100%; and (3) the lattice constants at 0 K tend to be smaller than those at room temperature, which can lead to an overestimation of the elastic moduli in the computational results.

The oxide electrolytes generally exhibited relatively high elastic moduli, with the Pugh's ratio B/G for most of them being less than 2.0. Specifically, their polycrystalline Young's moduli E generally ranged from 90 to 170 GPa, with the exception of Li_2SO_4 and the perovskite-type materials. Among these, Li_2SO_4, which contains both sulfur and oxygen, demonstrated unique elastic properties. Both α-Li_2SO_4 and β-Li_2SO_4 exhibited relatively low elastic moduli. Notably, α-Li_2SO_4 had an exceptionally high B/G value of 4.28, whereas the value of β-Li_2SO_4 was somewhat lower (B/G = 2.10). The α-phase of Li_2SO_4, which exhibits higher ionic conductivity than the β-phase, undergoes a phase transition from b to a at 577 °C, enhancing its ionic conductivity through the paddlewheel mechanism.[64]

While Li_2SO_4 alone is not widely recognized as a high-conductivity solid-state electrolyte at room temperature, its incorporation into Li_3BO_3-based glass and glass–ceramic electrolytes has been reported to enhance formability.[65] This improved formability is essential for achieving high-density electrolyte pellets, leading to higher ionic conductivity. The improved formability is particularly attributed to the ductility of Li_2SO_4. Previous studies have highlighted the relevance of Pugh's ratio (B/G) as an indicator of ductility, with materials exhibiting a Pugh's ratio greater than 1.75 generally regarded as ductile. In this study, α-Li_2SO_4 exhibited relatively high Pugh's ratios, suggesting their intrinsic ductility. Such ductile behavior is expected to promote more efficient compaction during the pressing process, leading to higher pellet densities.

Additionally, α-Li_2SO_4 exhibited a larger MAV compared to β-Li_2SO_4 and other oxide electrolytes, which was comparable to

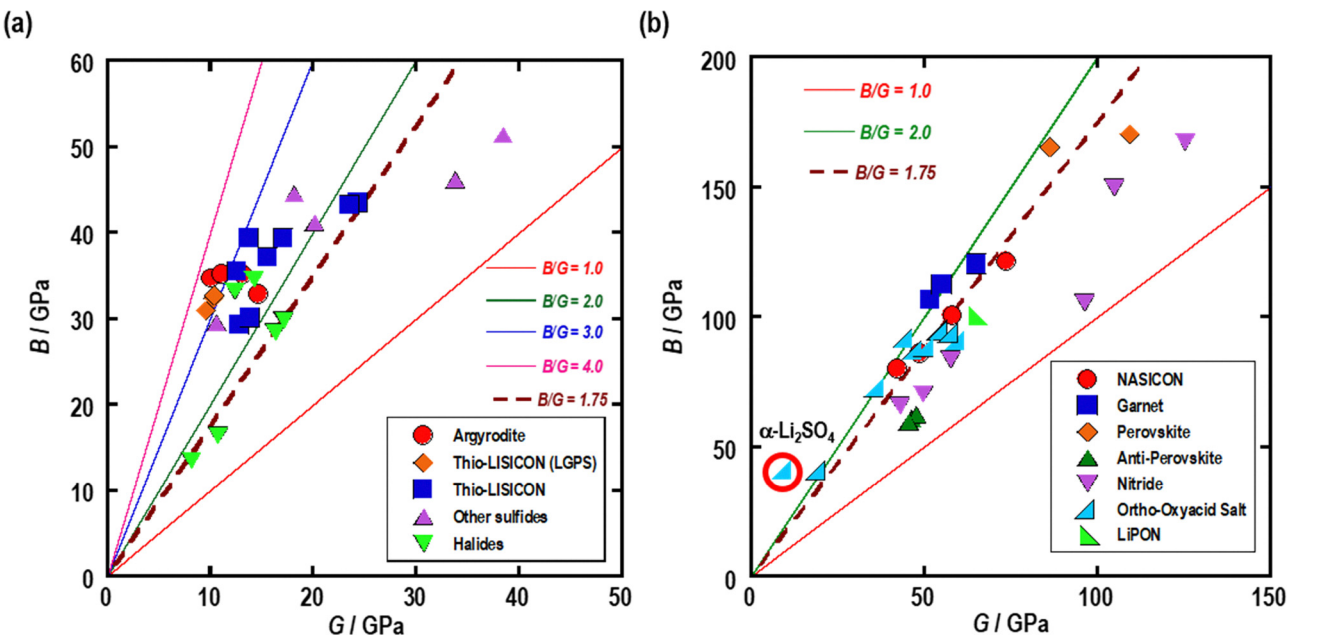

Fig. 1 Correlation between shear moduli G and bulk moduli B of various crystal structures of (a) sulfide and halide electrolytes, and (b) oxide and nitride electrolytes. The red circle in (b) refer to the plots for a-Li_2SO_4 crystal.

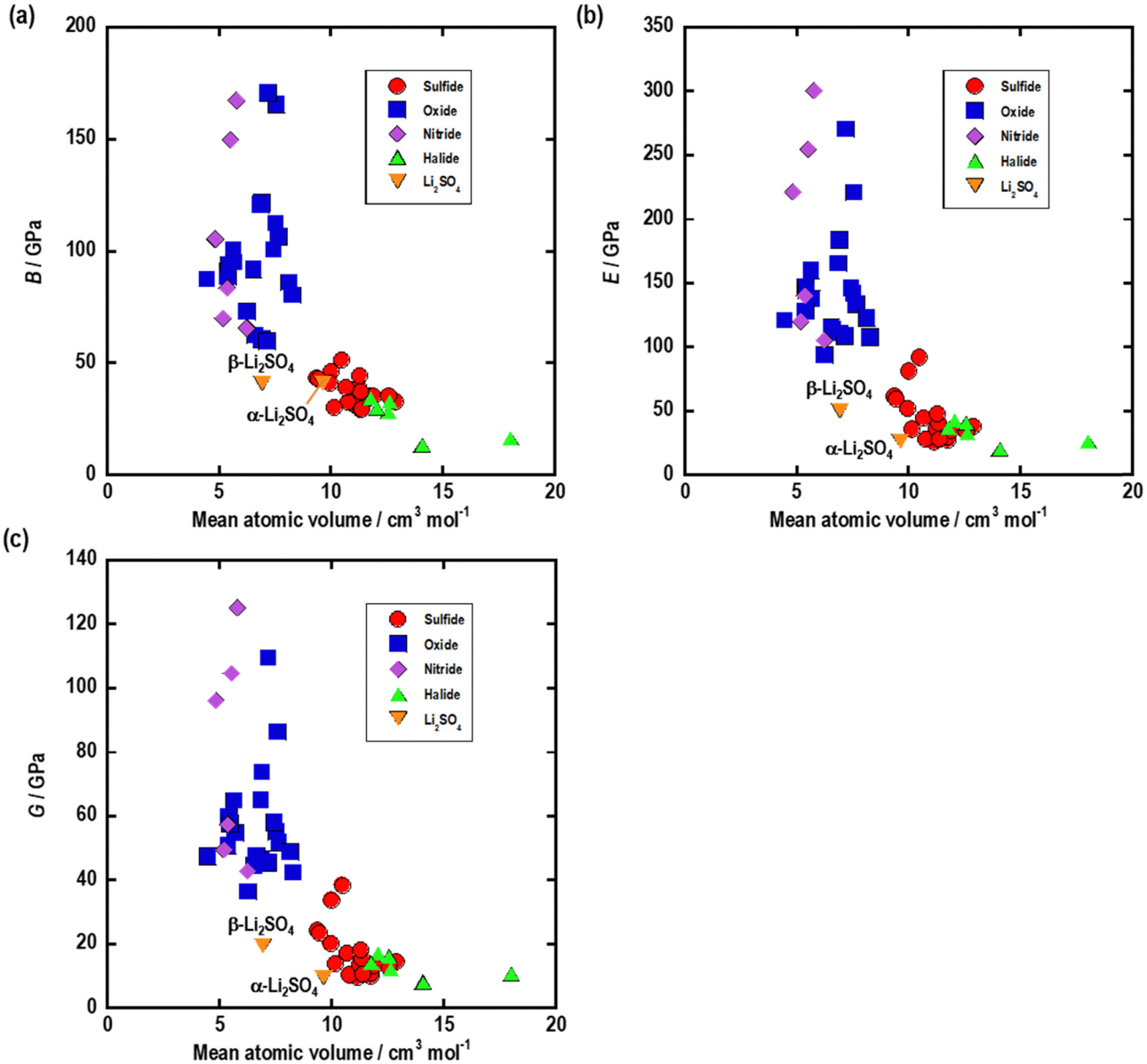

Fig. 2 Correlation between mean atomic volume and (a) bulk moduli B, (b) polycrystalline elastic moduli E, and (c) shear moduli G of various crystal structures of Li-ion conductors.

those of sulfides. This characteristic is thought to be a key factor contributing to its lower E and G values. Interestingly, the bulk moduli of α-Li_2SO_4 and β-Li_2SO_4 were nearly identical, despite the significant difference in their MAVs.

Perovskite-type structures generally displayed relatively high elastic moduli, with E values exceeding 200 GPa, B values of approximately 170 GPa, and G values of approximately 100 GPa. Moreover, anti-perovskite structures exhibited significantly lower B/G ratios (<1.5). These materials had relatively low bulk moduli (of approximately 60 GPa), contributing to their reduced B/G ratios.

Nitride electrolyte structures also displayed high elastic constants and low B/G ratios. Specifically, their B/G values (<1.5) were generally lower than those of oxides (~ 1.75). Among the nitrides, α-Li_3N exhibited relatively low elastic moduli (E = 105.79 GPa, B = 65.83 GPa, G = 42.93 GPa); however, these values were still higher than those of other electrolyte materials, particularly sulfides and halides. The elastic moduli of Li_7PN_4 and $LiSi_2N_3$ were comparable to those of perovskite oxides. Notably, the shear modulus of $LiSi_2N_3$ was approximately 125 GPa, marking the highest value among all materials analyzed in this study.

In contrast, the elastic moduli of halides were generally low and comparable to those of sulfides. Specifically, $LiAlCl_4$ exhibited significantly low elastic moduli (E = 20.37 GPa, B = 13.45 GPa, G = 8.16 GPa). However, their B/G ratios varied among the halide materials selected in this study. Notably, Li_2CdCl_4 had a higher Pugh's ratio (B/G = 2.68), suggesting that its ductility is comparable to that of several sulfide materials. In contrast, the B/G of Li_3MCl_6-type (M = Y, In) was approximately 1.75,

indicating that their ductility is not superior to that of sulfide materials. The elastic moduli of these materials were calculated in a previous study,[15] and their values were generally consistent with those reported in this study.

Fig. 1 shows the relationship between the calculated shear modulus (G) and bulk modulus (B) values from the computational results. Fig. 1(a) presents the results for sulfide and halide crystals, which generally exhibit relatively low elastic moduli. Most of their Pugh's ratios (B/G) are higher than 1.75 (above the brown dotted line), indicating that these electrolytes are likely to be ductile materials. The mechanical ductility of actual solid electrolytes (which are in the form of powder compacts) within a battery cannot be fully predicted solely based on the calculated Pugh's ratio. Fig. 1(b) shows the computation results for oxides and nitrides, which have higher elastic constants. All the oxides are generally distributed around B/G = 1.75 (within the range of 1.5–2.0), except for α-Li_2SO_4. By contrast, the nitrides are divided into two groups: those with B/G ratios of $\sim$1.75 and $<$1.75. Furthermore, the B/G ratio of α-Li_2SO_4, indicated by the red circle in the figure, is uniquely positioned compared to other materials.

Fig. 2 illustrates the relationship between MAV and (a) bulk modulus (B), (b) polycrystalline Young's modulus (E), and (c) shear modulus (G) in our computational results. The data indicate a negative nonlinear correlation between MAV and elastic constants across all electrolyte types. These correlations align with the relationship between MAV and Young's modulus observed in glass electrolytes reported by our group.[18] Oxide and nitride electrolytes typically have low MAV and high elastic moduli, while sulfides and halides exhibit the opposite trend, with high MAV and low elastic moduli. Notably, Li_2SO_4 displays a unique distribution in Fig. 2. Despite having an MAV similar to that of oxides, β-Li_2SO_4 shows elastic moduli comparable to those of sulfides. Moreover, the plot for α-Li_2SO_4 in Fig. 2 aligns within the distribution of sulfides, despite containing oxygen, showing elastic properties similar to sulfides that do not contain oxygen.

Notably, oxide and nitride electrolytes display a wide range of elastic constants even with similar MAV values. This suggests that factors beyond MAV, such as crystal structure and constituent elements, also play a significant role in determining the elastic moduli of nitrides and oxides. In contrast, the variation in elastic constants is relatively small for the sulfide and halide electrolytes selected in this study.

5. Conclusions

Elastic properties for the crystal structures of various sulfide, oxide, nitride, and halide solid electrolytes, including additive materials, were computationally predicted. Sulfide and halide electrolytes generally exhibited lower elastic moduli, whereas oxide and nitride electrolytes displayed higher values. Pugh's ratio (B/G), used to predict ductility or brittleness, was typically higher than 2 for sulfide and halide electrolytes. In contrast, the B/G ratios for oxide and nitride electrolytes were generally approximately 1.75 and $<$1.5, respectively. These results suggest that sulfide and halide electrolytes are more likely to possess ductility, whereas oxide and nitride materials tend to be more brittle. Notably, the α-Li_2SO_4 crystal structure exhibited an exceptionally high Pugh's ratio of 4.28, significantly higher than that of the other electrolytes. This computational result supports the mechanical ductility and formability observed in previous experimental studies. In addition, MAV was negatively correlated with the calculated elastic constants, and these negative nonlinear correlations were consistent with those observed for glass electrolytes. The oxide and nitride electrolytes exhibited significant variability in elastic moduli despite similar MAV values, highlighting the influence of crystal structure and constituent elements. These elastic modulus calculations are expected to assist in the selection and synthesis of solid electrolyte materials resistant to mechanical degradation.

Author contributions

Masato Torii: performed the simulations, processed the results, wrote the manuscript. Atsushi Sakuda: supervised the work, revised the manuscript. Kota Motohashi: provided critical feedback, revised the manuscript. Akitoshi Hayashi: provided critical feedback, revised the manuscript.

Conflicts of interest

The authors declare no conflict of interest.

Data availability

Furthermore, the elastic modulus data in CSV format as well as the elastic tensor data are available at GitHub at **https://github.com/MasatoTorii/Li_ElasticDB**.

Detailed information on the solid electrolyte materials used in this study and experimentally obtained elastic moduli of amorphous electrolytes prepared *via* mechanical milling are available in SI. See DOI: **https://doi.org/10.1039/d5ma00733j**

Acknowledgements

This study was supported by MEXT/JSPS KAKENHI Grant Number JP23H04633 and the 2024 Osaka Metropolitan University (OMU) Strategic Research Promotion Project (Priority Research). It was also partially funded by JST SPRING, Grant Number JPMJSP2139. First-principles calculations were partially conducted using computing resources provided by the Research Institute for Information Technology, Kyushu University, under the category of General Projects.

References

1 K. Takada, *Acta Mater.*, 2013, **61**, 759–770, DOI: **10.1016/j.actamat.2012.10.034**.

2 Y. Kato, S. Hori, T. Saito, K. Suzuki, M. Hirayama, A. Mitsui, M. Yonemura, H. Iba and R. Kanno, *Nat. Energy*, 2016, **1**, 16030, DOI: 10.1038/nenergy.2016.30.
3 J. Janek and W. G. Zeier, *Nat. Energy*, 2016, **1**, 16141, DOI: 10.1038/nenergy.2016.141.
4 A. Hayashi, A. Sakuda and M. Tatsumisago, *Front. Energy Res.*, 2016, **4**, 25, DOI: 10.3389/fenrg.2016.00025.
5 J. Lau, R. H. DeBlock, D. M. Butts, D. S. Ashby, C. S. Choi and B. S. Dunn, *Adv. Energy Mater.*, 2018, **8**, 1800933, DOI: 10.1002/aenm.201800933.
6 A. Sakuda, A. Hayashi and M. Tatsumisago, *Sci. Rep.*, 2013, **3**, 2261, DOI: 10.1038/srep02261.
7 N. Kamaya, K. Homma, Y. Yamakawa, M. Hirayama, R. Kanno, M. Yonemura, T. Kamiyama, Y. Kato, S. Hama, K. Kawamoto and A. Mitsui, *Nat. Mater.*, 2011, **10**, 682–686, DOI: 10.1038/nmat3066.
8 Y. Kato, S. Hori and R. Kanno, *Adv. Energy Mater.*, 2020, **10**, 2002153, DOI: 10.1002/aenm.202002153.
9 H. J. Deiseroth, S. T. Kong, H. Eckert, J. Vannahme, C. Reiner, T. Zaiss and M. Schlosser, *Angew. Chem., Int. Ed.*, 2008, **47**, 755–758, DOI: 10.1002/anie.200703900.
10 P. Adeli, J. D. Bazak, K. H. Park, I. Kochetkov, A. Huq, G. R. Goward and L. F. Nazar, *Angew. Chem., Int. Ed.*, 2019, **58**, 8681–8686, DOI: 10.1002/anie.201814222.
11 R. Murugan, V. Thangadurai and W. Weppner, *Angew. Chem., Int. Ed.*, 2007, **46**, 7778–7781, DOI: 10.1002/anie.200701144.
12 M. Kotobuki, H. Munakata, K. Kanamura, Y. Sato and T. Yoshida, *J. Electrochem. Soc.*, 2010, **157**, A1076, DOI: 10.1149/1.3474232.
13 B. A. Boukamp and R. A. Huggins, *Mater. Res. Bull.*, 1978, **13**, 23–32, DOI: 10.1016/0025-5408(78)90023-5.
14 T. Asano, A. Sakai, S. Ouchi, M. Sakaida, A. Miyazaki and S. Hasegawa, *Adv. Mater.*, 2018, **30**, e1803075, DOI: 10.1002/adma.201803075.
15 K. Kim, D. Park, H.-G. Jung, K. Y. Chung, J. H. Shim, B. C. Wood and S. Yu, *Chem. Mater.*, 2021, **33**, 3669–3677, DOI: 10.1021/acs.chemmater.1c00555.
16 R. Hill, *Proc. Phys. Soc., London, Sect. A*, 1952, **65**, 349–354, DOI: 10.1088/0370-1298/65/5/307.
17 S. F. Pugh, XCII, *Philos. Mag.*, 1954, **45**, 823–843, DOI: 10.1080/14786440808520496.
18 A. Kato, M. Nose, M. Yamamoto, A. Sakuda, A. Hayashi and M. Tatsumisago, *J. Ceram. Soc. Jpn.*, 2018, **126**, 719–727, DOI: 10.2109/jcersj2.18022.
19 Z. Deng, Z. Wang, I. H. Chu, J. Luo and S. P. Ong, *J. Electrochem. Soc.*, 2016, **163**, A67–A74, DOI: 10.1149/2.0061602jes.
20 P. Hohenberg and W. Kohn, *Phys. Rev.*, 1964, **136**, B864–B871, DOI: 10.1103/PhysRev.136.B864.
21 W. Kohn and L. J. Sham, *Phys. Rev.*, 1965, **140**, A1133–A1138, DOI: 10.1103/PhysRev.140.A1133.
22 G. Kresse and J. Furthmüller, *Phys. Rev. B:Condens. Matter Mater. Phys.*, 1996, **54**, 11169–11186, DOI: 10.1103/PhysRevB.54.11169.
23 G. Kresse and J. Furthmüller, *Comput. Mater. Sci.*, 1996, **6**, 15–50, DOI: 10.1016/0927-0256(96)00008-0.
24 J. P. Perdew, K. Burke and M. Ernzerhof, *Phys. Rev. Lett.*, 1996, **77**, 3865–3868, DOI: 10.1103/PhysRevLett.77.3865.
25 J. P. Perdew, K. Burke and M. Ernzerhof, *Phys. Rev. Lett.*, 1997, **78**, 1396, DOI: 10.1103/PhysRevLett.78.1396 [*Phys. Rev. Lett.*, 1996, **77**, 3865–3868].
26 P. E. Blöchl, *Phys. Rev. B:Condens. Matter Mater. Phys.*, 1994, **50**, 17953–17979, DOI: 10.1103/PhysRevB.50.17953.
27 G. Kresse and D. Joubert, *Phys. Rev. B:Condens. Matter Mater. Phys.*, 1999, **59**, 1758–1775, DOI: 10.1103/PhysRevB.59.1758.
28 H. J. Monkhorst and J. D. Pack, *Phys. Rev. B*, 1976, **13**, 5188–5192, DOI: 10.1103/PhysRevB.13.5188.
29 Z. Hu and H. Metiu, *J. Phys. Chem. C*, 2011, **115**, 5841–5845, DOI: 10.1021/jp111350u.
30 X. Lu, S. Wang, R. Xiao, S. Shi, H. Li and L. Chen, *Nano Energy*, 2017, **41**, 626–633, DOI: 10.1016/j.nanoen.2017.09.044.
31 S. Kc, R. C. Longo, K. Xiong and K. Cho, *Solid State Ionics*, 2014, **261**, 100–105, DOI: 10.1016/j.ssi.2014.04.021.
32 H. Kamisaka, T. Suenaga, H. Nakamura and K. Yamashita, *J. Phys. Chem. C*, 2010, **114**, 12777–12783, DOI: 10.1021/jp104355q.
33 S. Grimme, S. Ehrlich and L. Goerigk, *J. Comput. Chem.*, 2011, **32**, 1456–1465, DOI: 10.1002/jcc.21759.
34 V. Wang, N. Xu, J.-C. Liu, G. Tang and W.-T. Geng, *Comput. Phys. Commun.*, 2021, **267**, 108033, DOI: 10.1016/j.cpc.2021.108033.
35 T. Kimura, R. Izawa, C. Hotehama, K. Fujii, A. Sakuda, M. Yashima, M. Tatsumisago and A. Hayashi, *Solid State Ionics*, 2023, **399**, 116287, DOI: 10.1016/j.ssi.2023.116287.
36 Z. D. Hood, C. Kates, M. Kirkham, S. Adhikari, C. Liang and N. A. W. Holzwarth, *Solid State Ionics*, 2016, **284**, 61–70, DOI: 10.1016/j.ssi.2015.10.015.
37 S. T. Kong, O. Gün, B. Koch, H. J. Deiseroth, H. Eckert and C. Reiner, *Chemistry*, 2010, **16**, 5138–5147, DOI: 10.1002/chem.200903023.
38 P. Vinatier, P. Gravereau, M. Ménétrier, L. Trut and A. Levasseur, *Acta Crystallogr., Sect. C:Cryst. Struct. Commun.*, 1994, **50**, 1180–1183, DOI: 10.1107/S0108270193013630.
39 M. Murayama, R. Kanno, M. Irie, S. Ito, T. Hata, N. Sonoyama and Y. Kawamoto, *J. Solid State Chem.*, 2002, **168**, 140–148, DOI: 10.1006/jssc.2002.9701.
40 B. T. Ahn and R. A. Huggins, *Mater. Res. Bull.*, 1989, **24**, 889–897, DOI: 10.1016/0025-5408(89)90053-6.
41 T. Kimura, C. Hotehama, A. Sakuda, M. Tatsumisago and A. Hayashi, *RSC Adv.*, 2021, **11**, 25211–25216, DOI: 10.1039/d1ra03194e.
42 R. Kanno, T. Hata, Y. Kawamoto and M. Irie, *Solid State Ionics*, 2000, **130**, 97–104, DOI: 10.1016/S0167-2738(00)00277-0.
43 T. Kaib, S. Haddadpour, M. Kapitein, P. Bron, C. Schröder, H. Eckert, B. Roling and S. Dehnen, *Chem. Mater.*, 2012, **24**, 2211–2219, DOI: 10.1021/cm3011315.
44 T. Kimura, A. Kato, C. Hotehama, A. Sakuda, A. Hayashi and M. Tatsumisago, *Solid State Ionics*, 2019, **333**, 45–49, DOI: 10.1016/j.ssi.2019.01.017.
45 F. Zheng, M. Kotobuki, S. Song, M. O. Lai and L. Lu, *J. Power Sources*, 2018, **389**, 198–213, DOI: 10.1016/j.jpowsour.2018.04.022.

46 H. Aono, N. Imanaka, G.-Y. Adachi and H. Li, *Acc. Chem. Res.*, 1994, **27**, 265–270, DOI: **10.1021/ar00045a002**.
47 H. Y.-P. Hong, *Mater. Res. Bull.*, 1978, **13**, 117–124, DOI: **10.1016/0025-5408(78)90075-2**.
48 J. B. Bates, N. J. Dudney, G. R. Gruzalski, R. A. Zuhr, A. Choudhury, C. F. Luck and J. D. Robertson, *J. Power Sources*, 1993, **43**, 103–110, DOI: **10.1016/0378-7753(93)80106-Y**.
49 Y. Inaguma, C. Liquan, M. Itoh, T. Nakamura, T. Uchida, H. Ikuta and M. Wakihara, *Solid State Commun.*, 1993, **86**, 689–693, DOI: **10.1016/0038-1098(93)90841-A**.
50 Y. Zhao and L. L. Daemen, *J. Am. Chem. Soc.*, 2012, **134**, 15042–15047, DOI: **10.1021/ja305709z**.
51 M. Tatsumisago, R. Takano, K. Tadanaga and A. Hayashi, *J. Power Sources*, 2014, **270**, 603–607, DOI: **10.1016/j.jpowsour.2014.07.061**.
52 C. Okushima, Y. Yoneda, T. Kimura, K. Motohashi, A. Sakuda, M. Tatsumisago and A. Hayashi, *J. Ceram. Soc. Jpn.*, 2023, **131**, 141–145, DOI: **10.2109/jcersj2.23014**.
53 H. Yamane, S. Kikkawa and M. Koizumi, *Solid State Ionics*, 1987, **25**, 183–191, DOI: **10.1016/0167-2738(87)90119-6**.
54 W. Schnick and J. Luecke, *Solid State Ionics*, 1990, **38**, 271–273, DOI: **10.1016/0167-2738(90)90432-Q**.
55 H. D. Lutz, W. Schmidt and H. Haeuseler, *J. Phys. Chem. Solids*, 1981, **42**, 287–289, DOI: **10.1016/0022-3697(81)90142-6**.
56 H. D. Lutz, Z. Zhang and A. Pfitzner, (M^{II} Mn, Cd, Pb), *Solid State Ionics*, 1993, **62**, 1–3, DOI: **10.1016/0167-2738(93)90245-X**.
57 H. Maekawa, T. Iwatani, H. Shen, T. Yamamura and J. Kawamura, *Solid State Ionics*, 2008, **178**, 1637–1641, DOI: **10.1016/j.ssi.2007.10.018**.
58 X. Li, J. Liang, J. Luo, M. Norouzi Banis, C. Wang, W. Li, S. Deng, C. Yu, F. Zhao, Y. Hu, T.-K. Sham, L. Zhang, S. Zhao, S. Lu, H. Huang, R. Li, K. R. Adair and X. Sun, *Energy Environ. Sci.*, 2019, **12**, 2665–2671, DOI: **10.1039/C9EE02311A**.
59 J. C. Bachman, S. Muy, A. Grimaud, H.-H. Chang, N. Pour, S. F. Lux, O. Paschos, F. Maglia, S. Lupart, P. Lamp, L. Giordano and Y. S. Shao-Horn, *Chem. Rev.*, 2016, **116**, 140–162, DOI: **10.1021/acs.chemrev.5b00563**.
60 A. Jain, S. P. Ong, G. Hautier, W. Chen, W. D. Richards, S. Dacek, S. Cholia, D. Gunter, D. Skinner, G. Ceder and K. A. Persson, *APL Mater.*, 2013, **1**, 011002, DOI: **10.1063/1.4812323**.
61 G. Bergerhoff, R. Hundt, R. Sievers and I. D. Brown, *J. Chem. Inf. Comput. Sci.*, 1983, **23**, 66–69, DOI: **10.1021/ci00038a003**.
62 Z. Q. Wang, M. S. Wu, G. Liu, X. L. Lei, B. Xu and C. Y. Ouyang, *Int. J. Electrochem. Sci.*, 2014, **9**, 562–568, DOI: **10.1016/S1452-3981(23)07739-8**.
63 S. Yu, R. D. Schmidt, R. Garcia-Mendez, E. Herbert, N. J. Dudney, J. B. Wolfenstine, J. Sakamoto and D. J. Siegel, *Chem. Mater.*, 2016, **28**, 197, DOI: **10.1021/acs.chemmater.5b03854**.
64 A. Lundén, *Solid State Ionics*, 1988, **28–30**, 163, DOI: **10.1016/S0167-2738(88)80026-2**.
65 M. Tatsumisago, R. Takano, M. Nose, K. Nagao, A. Kato, A. Sakuda, K. Tadanaga and A. Hayashi, *J. Ceram. Soc. Jpn.*, 2017, **125**, 433, DOI: **10.2109/jcersj2.17026**.